

Wireless resonant circuits for the minimally invasive sensing of biophysical processes in magnetic resonance imaging

Aviad Hai¹, Virginia Ch. Spanoudaki², Benjamin B. Bartelle¹ and Alan Jasanoff^{1,3,4*}

Biological electromagnetic fields arise throughout all tissue depths and types, and correlate with physiological processes and signalling in organs of the body. Most of the methods for monitoring these fields are either highly invasive or spatially coarse. Here, we show that implantable active coil-based transducers that are detectable via magnetic resonance imaging enable the remote sensing of biological fields. These devices consist of inductively coupled resonant circuits that change their properties in response to electrical or photonic cues, thereby modulating the local magnetic resonance imaging signal without the need for onboard power or wired connectivity. We discuss design parameters relevant to the construction of the transducers on millimetre and submillimetre scales, and demonstrate their in vivo functionality for measuring time-resolved bioluminescence in rodent brains. Biophysical sensing via microcircuits that leverage the capabilities of magnetic resonance imaging may enable a wide range of biological and biomedical applications.

Biogenic electromagnetic fields underlie many of the most important processes of the body and form the basis of crucial biomedical technologies for monitoring and diagnosis^{1–4}. In nervous and muscular tissues, electrical potentials are essential for rapid intercellular communication and changes in cellular state^{5–7}. The measurement of such signals is fundamental to the study of healthy brain and muscle function, and the characterization of threatening dysfunctions such as those that occur in epilepsy or peripheral neuropathies^{8–10}. Many chemical processes can also be converted into electromagnetic signals using electrochemical techniques. In both preclinical research and clinical settings, such strategies are the basis for monitoring tissue variables ranging from pH in tumours^{11,12} to neurochemical disruptions in Parkinson's disease^{13–15}. Although visible photonic signals do not arise endogenously in mammals, the detection of such signals in deep tissue is the basis for studies of gene expression and biochemical activity via bioluminescent and chemiluminescent reporters in animal models^{16,17}. A minimally invasive technology for the improved measurement of optical signals near their origin could vastly expand the range of physiological phenomena accessible to monitoring.

Despite the significance of electromagnetic signal sources in biomedicine, tools for measuring electric, magnetic and photonic events in tissue are limited. Macroscopic fields arising from gross muscle contraction and synchronized neural activity can be measured using techniques such as electromyography, electroencephalography and magnetoencephalography^{1–7}, but these methods lack sensitivity in localizing signal origins and cannot discern events at the cellular or near-cellular scale. Probes based on glass micropipettes and metal electrodes can be used to record electrical events at a single-cell level from neurons and cardiomyocytes in freely moving animals, however, they require invasive and technically difficult spatial targeting^{18,19}. Microfabricated arrays of electrodes provide multiplexed recordings of extracellular electrical signals

from tens or hundreds of locations in human subjects^{20,21}, but also target relatively few points in space and commonly require invasive, wired connectivity. Although minimally invasive optical technologies are available for wide-field, high-resolution neurophysiological recordings through thinned skull in rodents^{22,23}, these methods are not easily translatable to primates and cannot reliably measure signals below a depth of about 1 mm. These limitations, coupled with the danger of chronic and acute adverse reactions to both electrical and optical wired probes, highlight the need for minimally invasive approaches to the detection of biomedically relevant electromagnetic fields in opaque tissue.

Probe technologies that interact with non-invasive imaging modalities offer an enticing alternative to more traditional approaches for tetherless detection of electromagnetic fields in biological systems. By converting fields at their sites of origin to changes in localized imaging signals, such probes can avoid the need for powered transmission of information out of the tissue. One demonstration of this type of strategy employed piezoelectric microcircuits to sense neural activity by converting bioelectric events to ultrasonic waves detectable by a remote transducer^{24,25}. To overcome the attenuation of ultrasound by bone, brain applications may rely on a subdural receiver to amplify the deep tissue signals and convert them to radiofrequency signals for recording outside the body²⁴. Molecular probes suitable for magnetic resonance imaging (MRI)-mediated detection of electromagnetic events have also been introduced. They exploit the superior depth penetration and robustness of MRI-based detection methods. In vitro studies have reported the detection of electric field fluctuations using a hydrogel-based MRI contrast agent²⁶, as well as photon detection using light-sensitive imaging agents^{27,28}. An important goal in adapting MRI-based probes for in vivo use is to improve their sensitivity to biologically relevant electromagnetic stimuli. In this regard, a microfabricated imaging agent that uses circuit-based amplification mechanisms to

¹Department of Biological Engineering, Massachusetts Institute of Technology, Cambridge, MA, USA. ²Koch Institute for Integrative Cancer Research, Massachusetts Institute of Technology, Cambridge, MA, USA. ³Department of Brain and Cognitive Sciences, Massachusetts Institute of Technology, Cambridge, MA, USA. ⁴Department of Nuclear Science and Engineering, Massachusetts Institute of Technology, Cambridge, MA, USA.

*e-mail: jasanoff@mit.edu

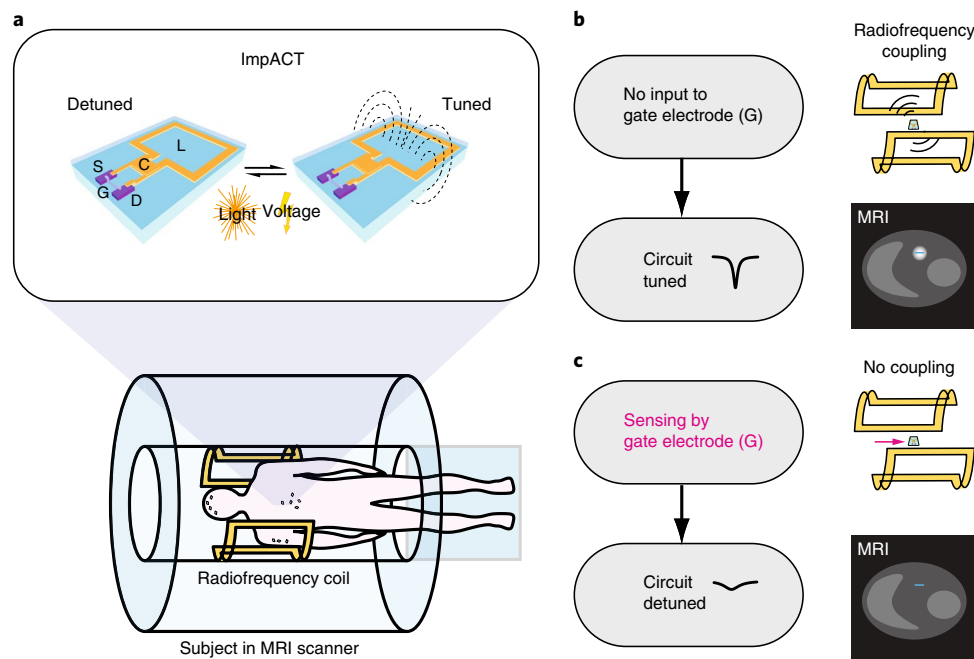


Fig. 1 | ImpACTs as imaging probes for functional MRI. **a**, ImpACTs are inductively coupled sensing circuits consisting of a FET (S, source; D, drain; G, gate) in parallel with an inductor (L) and capacitor (C). Light or voltage inputs to the gate tune or detune the device, thus altering the MRI signal (top). ImpACTs are designed to act as implantable sensors that can be detected by conventional MRI, potentially in human subjects (bottom). Each ImpACT harvests power from the scanner's radiofrequency coil and produces local signal changes modulated by electromagnetic input. **b**, Operation of an ImpACT tuned to the MRI scanner's resonance frequency, in the absence of input (left). Inductive coupling between the scanner's main radiofrequency coil and the ImpACT (top right) allows the device to produce local enhancement in MRI scans (bottom right; blue line denotes ImpACT position). **c**, Input to the ImpACT gate electrode detunes the radiofrequency circuit of the device (left), eliminating inductive coupling with the main coil (top right) and causing no MRI signal enhancement near the device (bottom right).

convert biophysical signals into MRI-detectable magnetic or radiofrequency signatures could constitute an attractive strategy for measuring electromagnetic events in living subjects.

To implement such an approach, we here introduce the concept of implantable active coil-based transducers (ImpACTs), which are designed for the wireless reporting of optical and electrical events in deep tissue without the need for onboard power, in conjunction with MRI-based detection and localization. ImpACTs are millimetre- or submillimetre-scale implantable devices that function like miniaturized variants of a standard circuit (a radiofrequency coil) that stimulates and detects MRI signals from a subject. In response to biological electromagnetic stimuli such as voltage or photonic input, the coils become actively tuned or detuned, changing their resonance characteristics and therefore their ability to couple inductively to the main MRI detection hardware, a large radiofrequency antenna that either sits over an area of interest (surface coil) or around the subject (volume coil). The strength of coupling between each ImpACT and the main coil, along with the duration and strength of radiofrequency impulses applied to the main coil, determines how bright the local MRI signal near the ImpACT will appear in an image and therefore provides the basis for an MRI-based readout of localized biophysical signals.

The ImpACT devices are fabricated as modified thin-film inductor–capacitor circuits. Tuning changes are actuated by altering the gate-source voltage (V_{GS}) across a field-effect transistor (FET) placed in parallel with the other circuit elements (Fig. 1). Changes to V_{GS} close or open the FET, shunting current to or from the coil's inductor and capacitor and altering the performance of the circuit. In this context, the ImpACT gate electrode acts as a sensor and can be rendered responsive to almost any electromagnetic signal of interest, relying on the same principles of commonly used, tethered FET-based biosensors that can sense electrophysiological

activity^{29,30}, light^{31,32} and biochemical analytes^{33–35}. In each case, the inductor element of the circuit can be used to harvest the radiofrequency energy needed to produce a sufficiently large drain-source voltage (V_{DS}) for the device to be in open mode without any bias voltage. We reasoned that such architectures could therefore provide a versatile basis for the rapid detection of a variety of physiological events by MRI.

Results

Theoretical characteristics of ImpACT devices. To explore the potential of ImpACTs to sense biologically relevant signals, we began by modelling their predicted responses to realistic biophysical signal sources. Biophysical potentials range from tens to hundreds of microvolts in the case of neuronal extracellular field potentials and reach tens of millivolts in the case of muscle contraction, cardiac activity, neuromuscular synaptic events and oscillations in the central nervous system²¹. Meanwhile, photonic signals generated by luminescent cell lines and animal models attain flux values of 10^{10} photons per second (p s^{-1}) or more, depending on which luminescent reporter is used and on the factors that regulate its activity^{17,36,37}. To test the prospects of detecting such signals, we simulated the response of the devices as a function of three key parameters: (1) the input signal introduced at the FET gate electrode, simulated as a change in the source–drain conductance of the FET due to alteration of its gate-source voltage (V_{GS}) or to the photonic input when using a photosensitive FET (photoFET); (2) the diameter of the ImpACT device's inductor (d), which determines its overall size and (3) the thickness of the metal film (t_m) used in the circuitry of the device.

The simulation model consisted of a circuit equivalent to the ImpACT device inductively coupled to a circuit representing a typical transmit–receive MRI volume coil (Fig. 2a). The ImpACT frequency response is measured as a tuning curve—the graph of the

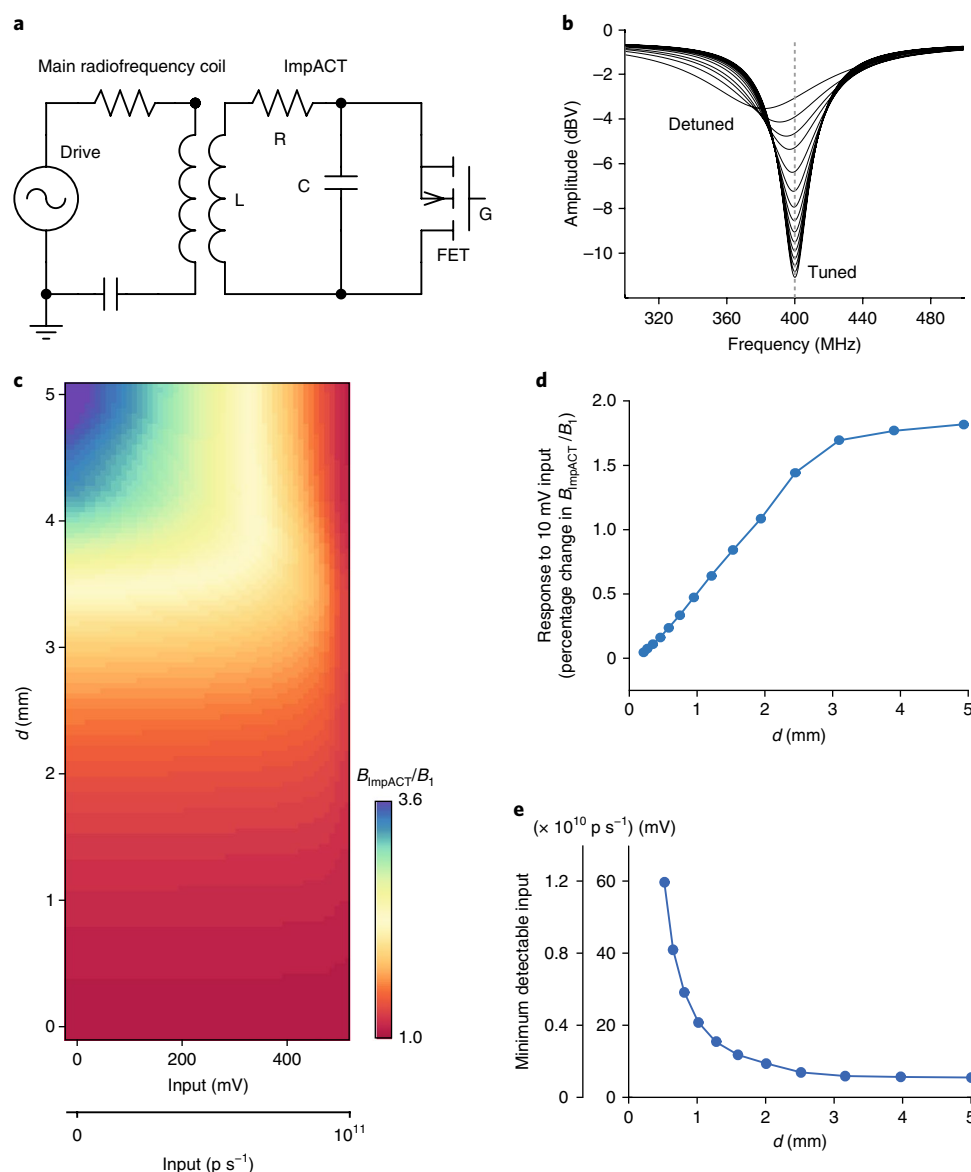


Fig. 2 | Theoretical performance of ImpACT designs. **a**, Equivalent circuit used for the simulation of ImpACT devices (right) coupled to the main radiofrequency coil of an MRI scanner (left). Radiofrequency pulses generated by the scanner drive the ensemble. R, resistor; L, inductor; C, capacitor; G, FET gate terminal. **b**, ImpACT tuning curve simulations as a function of voltage input that causes the device to vary between fully tuned and fully detuned states. **c**, Relative enhancement of local radiofrequency amplitude as a function of the ImpACT’s inductor diameter (d) and input strength in mV or p s^{-1} . Radiofrequency field enhancement by the ImpACT is expressed as B_{ImpACT}/B_1 , which translates directly into an increase in flip angle during the application of an MRI pulse via the scanner’s main coil. **d**, Response to a 10 mV input (equivalent to $2 \times 10^9 \text{ p s}^{-1}$), compared with zero input, as a function of the ImpACT inductor diameter. Changes in B_{ImpACT}/B_1 of $\geq 1\%$ are likely to be detectable in imaging. **e**, Minimum photonic and voltaic input signals predicted to produce a change $\geq 1\%$ in B_{ImpACT}/B_1 , compared with zero input, as a function of the device diameter.

radiofrequency signal reflected from the main MRI radiofrequency coil versus transmission frequency (Fig. 2b). The minimum of the curve indicates the ImpACT’s tuning frequency (ν) and the ratio of ν to the full width at the half height of the curve is the quality factor (Q) of the device. The ImpACT transmits the highest power when its Q is maximized and its frequency matches that of the MRI radiofrequency transmit–receive coil. In our simulations, the ImpACT is initially tuned to the resonance frequency of 400 MHz, corresponding to an MRI operating magnetic field strength (B_0) of 9.4 T. Opening the FET or photoFET thus detunes the circuit. The response properties of these active elements were assumed to follow typical current–voltage characteristics and were set according to the specifications of sensitive commercially available FET devices used

in our subsequent experiments. The source–drain resistance across the transistor falls from a value of $5 \text{ k}\Omega$ in the FET’s closed state to a value of $0.2 \text{ k}\Omega$ in the FET’s open state. Transitions between these values occur over an interval ranging between $\Delta V_{\text{GS}} = 0$ and 500 mV , where ΔV_{GS} is the difference between V_{GS} and the threshold voltage for FET opening, V_{th} .

Figure 2b illustrates the shift in the tuning curve as a function of ΔV_{GS} for a representative simulation of an ImpACT with single–turn inductor diameter of 10 mm and $t_m = 10 \mu\text{m}$. The tuned curve (low ΔV_{GS}) displayed Q of 17.7, whereas the detuned curve (high ΔV_{GS}) displayed a Q of 4.5. This corresponds to an input–dependent 8.6 dBV (2.7–fold) change in the transmission efficiency through the ImpACT device.

Expected dynamic range and sensitivity in MRI. To predict how ImpACT tuning changes could affect actual MRI signals, we next used our simulation approach to estimate the strength of the local radiofrequency field induced in the ImpACT by the main coil in a realistic imaging scenario. The ratio of the ImpACT's local field (B_{ImpACT}) to the field strength produced by the radiofrequency coil of the scanner (B_1) provides an approximate measure of the local MRI signal amplification expected at the ImpACT location (see Methods for details).

Figure 2c depicts B_{ImpACT}/B_1 as a function of voltage or photonic input amplitude for ImpACT devices with a range of diameters and $t_m = 10 \mu\text{m}$. For ImpACTs with $d = 1, 3$ and 5 mm at zero input, the values of B_{ImpACT}/B_1 are 1.2, 1.8 and 3.6, respectively; the B_{ImpACT}/B_1 values fall to 1.1, 1.3 and 1.1, respectively with a 500 mV input (10^{11} p s^{-1}), reflecting a strong size dependence of the device performance characteristics. These numbers correspond to stimulus-dependent modulation of up to 70% for the largest devices across the full range of input strengths we examined (Supplementary Fig. 1). For each ImpACT, the changes in B_{ImpACT}/B_1 are approximately linearly proportional to inputs in the $0\text{--}300 \text{ mV}$ range, equivalent to luminescent inputs of $0\text{--}1.7 \times 10^{10} \text{ p s}^{-1}$ falling on the 0.09 mm^2 photoFET light sensor we modelled. For inputs greater than 300 mV or $1.7 \times 10^{10} \text{ p s}^{-1}$, the predicted ImpACT responses become increasingly nonlinear; they reach an asymptote by input levels of 500 mV or 10^{11} p s^{-1} , at which point the FET or photoFET component is fully open and the ImpACT cannot be further detuned. These input levels thus establish an upper bound on the dynamic range of the devices.

To estimate the ImpACT responses to small biological-scale inputs, we predicted the modulations in B_{ImpACT}/B_1 expected to arise from inputs of 10 mV or $2 \times 10^9 \text{ p s}^{-1}$, compared to zero input (Fig. 2d). For ImpACTs with $d = 0\text{--}3 \text{ mm}$, the modelled signal change varies linearly in proportion to the device size; above $d = 3 \text{ mm}$, sensitivity to 10 mV inputs reaches a plateau, with expected modulations of about 1.6% in B_{ImpACT}/B_1 . We also estimated the minimum detectable ImpACT input, operationally defined as the voltage or photonic amplitude required to produce a 1% change in B_{ImpACT}/B_1 from its base value (Fig. 2e); this definition is justified by the fact that functional MRI experiments commonly detect imaging signal changes of about this magnitude or larger. On the basis of this criterion, we predicted that a 5 mm single-turn ImpACT could sense inputs as low as 5.4 mV , which is comparable to extracellular electrical potentials, and that a 1 mm device could sense inputs of at least 20.8 mV , which is comparable to transmembrane voltages in single cells. Devices of $d = 1 \text{ mm}$ and 5 mm could also detect photonic inputs of $4.2 \times 10^9 \text{ p s}^{-1}$ and $1.1 \times 10^9 \text{ p s}^{-1}$, respectively. With changes to the t_m , FET transconductance and the number of turns, additional sensitivity improvements or reductions in device dimensions could be possible; sensitivity to inputs below 10 mV are predicted for multi-turn ImpACTs as small as $250 \mu\text{m}$ in diameter (see Supplementary text and Supplementary Figs. 2–4).

Validation of ImpACTs in MRI. To validate our simulations and verify the ability of an actual ImpACT to undergo stimulus-dependent changes in tuning in an experimental setting, we constructed a series of single-turn thin-film FET-gated circuits. A device with $d = 3 \text{ mm}$ and $t_m = 10 \mu\text{m}$ is shown in Fig. 3a and labelled in Fig. 3b. A second ImpACT with dimensions matching the model parameters of Fig. 2b ($d = 10 \text{ mm}$) was used for the experimental validation of the predicted tuning behaviour. Using a network analyser inductively coupled to the device, we measured the frequency response over a range of ΔV_{GS} values (Fig. 3c). The behaviour of this ImpACT closely paralleled the simulated results, with Q values of 17.9 and 4.5 in the fully tuned and detuned states, respectively, almost exactly matching the model calculations. To probe the sensitivity of the device, we then examined the ImpACT's response to

the millivolt-scale inputs most relevant to biophysical phenomena. Inputs with $\Delta V_{\text{GS}} = 0\text{--}90 \text{ mV}$ in 10 mV increments all produced discernible changes in the ImpACT tuning curve (Fig. 3d). The responses are equivalent to an average change in reflected amplitude by $0.61 \pm 0.11 \text{ dBV}$ per 10 mV input increment, which indicates that millivolt-scale inputs are easily detectable.

The performance characteristics indicated by the tuning curves of Fig. 3c,d apply to the behaviour of ImpACT devices during steady-state radiofrequency irradiation but imaging applications would require the ImpACT to be functional during highly transient radiofrequency pulses typical of MRI scanner operation. To test the functionality and sensitivity of the ImpACT device in imaging, we performed MRI of FET- and photoFET-based ImpACT devices during modulation of their voltage or photonic input. The devices were placed inside a 78 mm diameter MRI transmit–receive coil while a simple MRI gradient echo-pulse sequence with an excitation pulse width of 1 ms and flip angle of 30° was applied. Parallel changes in tuning and image intensity could be obtained across wide dynamic ranges using both types of input (Supplementary Fig. 5). Representative results obtained using a photosensitive ImpACT constructed with $d = 3 \text{ mm}$ and $t_m = 10 \mu\text{m}$ are shown in Fig. 3e. The device was tuned to the MRI scanner's operating frequency of 400 MHz in the absence of input; under this condition, the MRI signal proximal to the inductor element of the circuit was $30.4 \pm 4.7\%$ higher than the water signal distal to the device, reflecting local intensification of radiofrequency flux by the ImpACT in its tuned state. When an input of $1 \times 10^{11} \text{ p s}^{-1}$ was applied, the MRI signal enhancement near the ImpACT diminished to only $5.6 \pm 2.7\%$ over baseline, a significant input-dependent decrease (t -test $P < 0.005$ over the $n = 8$ closest image pixels).

To examine the probable specificity of the ImpACT-mediated MRI signal to input-dependent modulations, we examined the sensitivity of the ImpACT to the extraneous environmental factors that could vary in realistic contexts. We performed measurements over a range of buffer dilutions to quantify the effect of different ion concentrations in the vicinity of the 3 mm ImpACT (Supplementary Fig. 6a). The results indicate that at salt concentrations relevant to serum or cerebrospinal fluid (150 mM and above), ImpACT tuning varies by only 0.05% per millimolar change in ion concentrations, meaning that dramatic fluctuations of over 10 mM in ionic strength would be required to produce MRI changes comparable to those elicited by even the smallest detectable voltage or photonic inputs. Similarly, ImpACT responses to temperature variation were minimal. Even across an unphysiologically large range of temperatures from about 22°C to 37°C , the experimentally determined tuning characteristics as a function of input are hardly affected (Supplementary Fig. 6b). The B_0 field of the MRI scanner is another environmental parameter that can vary, typically on the order of ten parts per million³⁸, primarily due to spatial variations in magnetic susceptibility in tissue. To model such effects, we examined the ImpACT's response to tuning offsets by up to 1 MHz from the main B_0 resonance frequency and showed that under all conditions the tuning behaviour as a function of input remains virtually unchanged (Supplementary Fig. 6c). Local B_1 fields produced by the scanner's main coil can also vary in realistic scanning conditions. However, such inhomogeneities are not expected to affect the interpretability of ImpACT-mediated responses because the ImpACT's signal enhancement simply scales with whatever the local B_1 is (see Fig. 2 and Supplementary Figs. 1 and 2). Differences in the angular orientation of an ImpACT could affect inductive coupling to the main coil and thus alter the magnitude of signal enhancements, but even these would not affect the profile of relative ImpACT responses to inputs of varying amplitude.

Performance of ImpACTs in clinically relevant settings. The initial assessment of our ImpACT devices was performed at a field

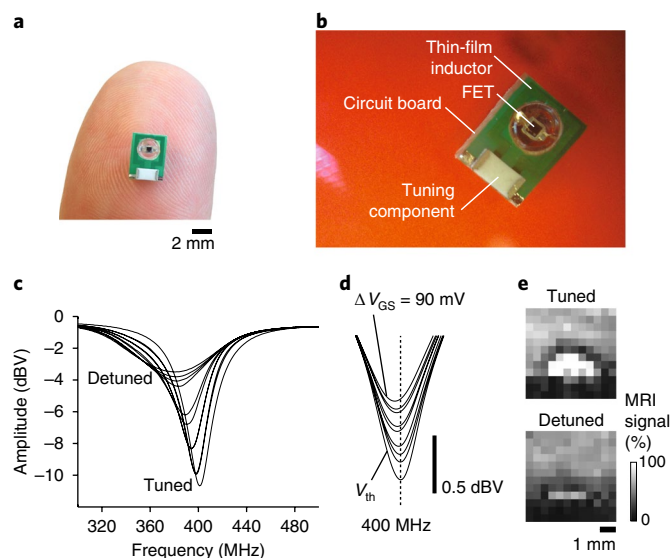


Fig. 3 | Tuning and imaging performance of an ImpACT prototype. **a**, An ImpACT fabricated using standard printed-circuit methods, with a $10\ \mu\text{m}$ layer of gold-plated copper as a conductive thin-film inductor of diameter $3\ \text{mm}$, connected in parallel to an FET sensor and a tuning component, to enable an initial resonance frequency at $\nu = 400\ \text{MHz}$. **b**, Close-up view of the ImpACT in **a** with the components labelled. **c**, Network analyser measurements demonstrating the ImpACT tuning curves over the full range of FET modulation. FET input was modulated from low ΔV_{GS} ($V_{\text{GS}} = V_{\text{th}}$) to high ΔV_{GS} ($V_{\text{th}} + 1\text{V}$), resulting in a 3.9-fold decrease in Q , from 17.9 to 4.5, which is comparable to the simulated values in Fig. 2. **d**, Modulation of the ImpACT tuning curve in response to millivolt-scale voltage inputs. The interval between adjacent curves is $10\ \text{mV}$. **e**, Modulation of the MRI signal by light-gated detuning of a photoFET-based ImpACT juxtaposed with a water-based phantom. The MRI signal in the absence of input (top) is approximately 30% higher than in the presence of input (bottom).

strength of $9.4\ \text{T}$, but potential clinical applications would probably involve considerably lower B_0 fields. To test ImpACT performance at a clinically relevant magnetic field strength, we constructed a $3\ \text{mm}$ ImpACT tuned for operation in a $3\ \text{T}$ MRI scanner and compared its performance with the results obtained at $9.4\ \text{T}$ (Supplementary Fig. 7). The experimental dynamic range is similar at both field strengths, although the ImpACT response reaches an asymptote at a lower input strength at lower field ($400\ \text{mV}$ versus $500\ \text{mV}$). The modelled performance of ImpACT devices as a function of field strength (Supplementary Fig. 7c) shows that the minimum detectable signal also increases at lower field. At $3\ \text{T}$, an ImpACT with $d = 3\ \text{mm}$ and $t_{\text{m}} = 10\ \mu\text{m}$ is predicted to detect $14.6\ \text{mV}$ or $2.9 \times 10^9\ \text{p s}^{-1}$ inputs, whereas a similar device tuned to operate at $9.4\ \text{T}$ could detect weaker inputs of $6.4\ \text{mV}$ or $1.3 \times 10^9\ \text{p s}^{-1}$.

A limitation of the application of some implantable electronic devices in biomedical settings is the propensity of such devices to deposit energy into biological tissue, which leads to local heating and potential damage. The amount of energy deposition depends on an interaction among multiple device- and tissue-dependent factors that together determine the specific absorption rate (SAR). A simple upper bound on the SAR for an ImpACT device can be calculated by determining the total power dissipated in the ImpACT itself and normalizing this by the tissue volume likely to be affected by each individual device, here approximated as a sphere equal to twice the device diameter. To compute this quantity, we used our simulation approach to determine the peak instantaneous power deposition, assuming operation at $400\ \text{MHz}$ with a typical main coil radiofrequency field strength ($B_1 = 2\ \mu\text{T}$). We found that the upper bounds on SAR ranged from $8 \times 10^{-3}\ \text{W kg}^{-1}$ for a $1\ \text{mm}$ device to $3 \times 10^{-4}\ \text{W kg}^{-1}$ for a $5\ \text{mm}$ device (Supplementary Fig. 8). Using a $3\ \text{mm}$ ImpACT operated continuously for $2\ \text{h}$ with a pulse sequence repetition time of $2\ \text{s}$ in contact with a $1\ \text{ml}$ buffer sample, we found that mean temperature rose by a maximum of about $1\ ^\circ\text{C}$, indicating a combined power deposition from the main B_1 coil and the ImpACT of less than $6 \times 10^{-4}\ \text{W}$ across the specimen. Such values

fall well within the safety margins of several W kg^{-1} specified by the US Food and Drug Administration³⁹ and indicate that ImpACT devices will be safe for use in animals and people.

ImpACT-based detection of bioluminescence in vitro and in vivo.

To examine the performance of an ImpACT device in biological settings, we attempted to modulate ImpACT-mediated MRI signals using biogenic sources. We chose to focus initially on bioluminescent detection (Fig. 4a) because this modality does not require electrical contact between the sensor and the specimen being measured. Using the photosensitive ImpACT device with $d = 3\ \text{mm}$, we began by examining the MRI signal when the device was stimulated by a $7.8\ \mu\text{M}$ luciferase solution after the addition of $1\ \text{mM}$ D-luciferin and $1\ \text{mM}$ adenosine triphosphate (ATP). The enzymatic reaction generated sufficient light flux to detune the device, producing an MRI signal decrease of $16 \pm 7\%$ with respect to the signal observed in the absence of luciferase (Fig. 4b). Minimal MRI signal changes of only $0.4 \pm 5.4\%$ were measured in the presence of luciferase, but without luciferin or ATP. Using network analyser measurements, we verified that the luciferase-mediated response in Fig. 4b was caused by detuning of the ImpACT; luciferase activity decreased the Q value of the device by $3.8 \pm 0.8\%$ and induced a tuning frequency shift of $2.7\ \text{MHz}$ (Fig. 4c).

These measurements demonstrate the ability of the ImpACT design to transduce bioluminescence signals to an MRI-detectable signal change. We next sought to determine whether endogenously expressed luciferase inside cells could produce similar effects. HEK293 cells expressing an engineered luciferase (NanoLuc) were placed in proximity to the $3\ \text{mm}$ ImpACT. After the addition of the luciferin analogue furimazine, a $3.6 \pm 0.6\%$ decrease in MRI signal that persisted for more than $1\ \text{h}$ was observed (Supplementary Fig. 9). No signal change was observed distally to the device.

Cellular expression of luciferase is widely used in vivo as a reporter for cell density and status in animal models of tumorigenesis and transplantation; we therefore investigated whether an

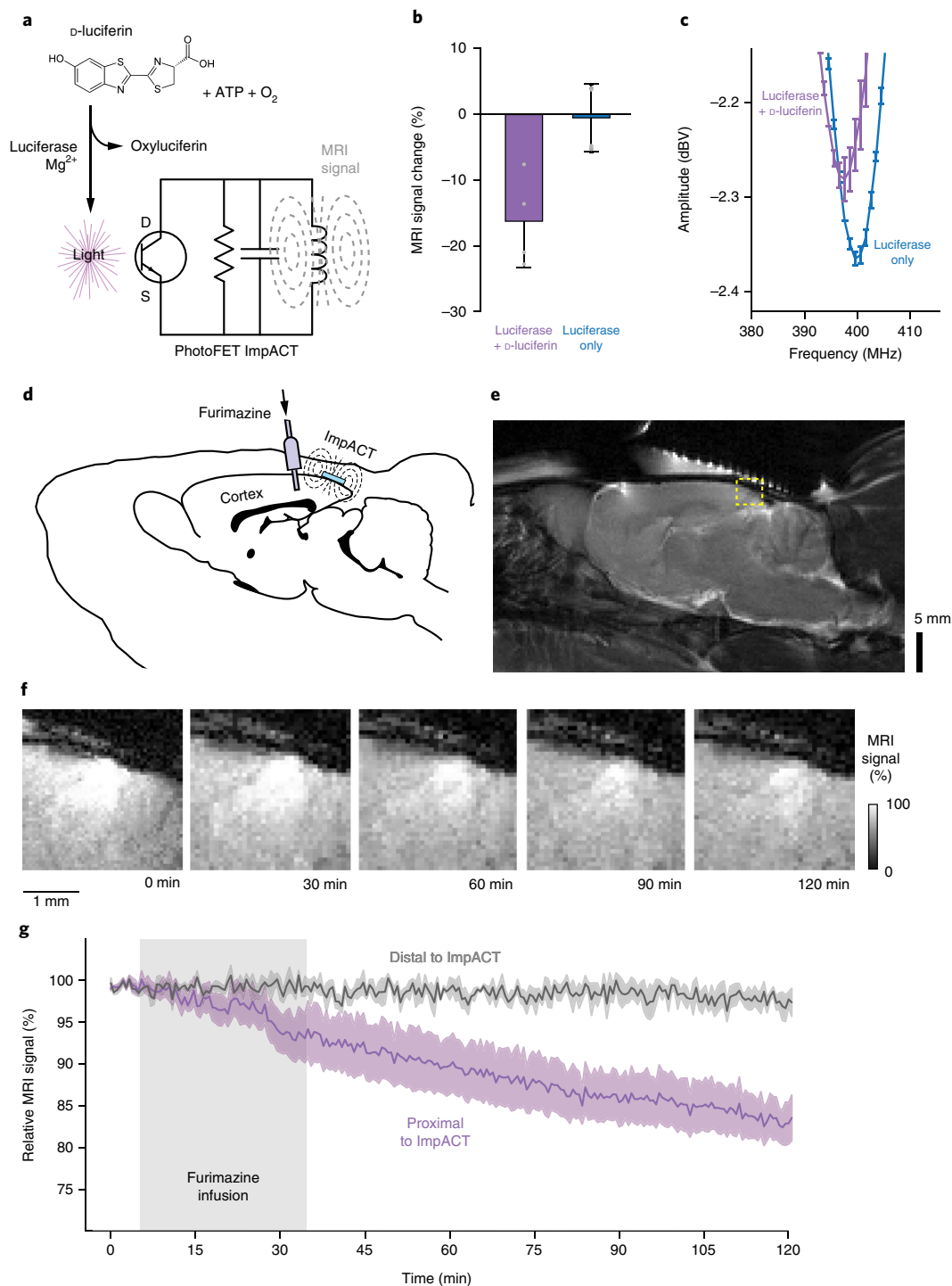


Fig. 4 | ImpACT-mediated detection of bioluminescence in vitro and in vivo. **a**, Schematic of bioluminescence detection by a photosensitive ImpACT. Luciferase in the presence of magnesium ions catalyses the conversion of *D*-luciferin, ATP and O_2 into oxyluciferin and light that acts on the gate terminal of the ImpACT's photoFET (bottom), thus altering the resonance properties and MRI signal. **b**, Average MRI signal changes measured using a 3 mm photosensitive ImpACT in the presence of 7.8 μM luciferase with (left) or without (right) the addition of *D*-luciferin. The MRI results are reported as the difference from the baseline image intensity distal to the ImpACT. Error bars denote s.e.m. ($n = 4$); the individual measurements are indicated by grey dots. **c**, Measurements of frequency response in the presence and absence of *D*-luciferin confirm that light production affects the MRI signal by detuning the device. Error bars denote s.e.m. ($n = 4$). **d**, ImpACT-mediated MRI monitoring of bioluminescent cells in live rat brains. Engineered luciferase (NanoLuc)-expressing HEK293 cells were grafted into the cerebral cortex. A device was implanted above the cells and a cannula inserted nearby for infusion of the NanoLuc substrate furimazine. **e**, Anatomical MRI scan of a rat brain showing the region of image signal modulated by the ImpACT (dashed yellow box). **f**, Close-up images obtained at $t = 0, 30, 60, 90$ and 120 min. The images capture the region before, during and after furimazine infusion, which occurred at $t = 5\text{--}35$ min. Signal enhancement in the centre of this region reflects the presence of the tuned ImpACT device; the enhancement dims over time as the ImpACT is progressively detuned by luminescence from the implanted cells. **g**, Mean time courses of relative MRI signal proximal (purple) and distal (grey) to the ImpACT (shaded intervals denote s.e.m.; $n = 4$). The furimazine infusion period is indicated by the grey box. Control experiments with injections lacking furimazine showed no discernable signal changes (Supplementary Fig. 10).

ImpACT could reveal the presence of luciferase-expressing cells in a living animal. NanoLuc-expressing HEK293 cells were xenografted into the cerebral cortex of anaesthetized rats and 3 mm ImpACT devices were implanted over the cells (Fig. 4d,e). MRI scanning was performed before, during and after intracranial injection of 1 mM furimazine substrate (3 μ l) proximal to the cell implantation sites. During injection and spreading of the furimazine in the brain parenchyma, we observed a significant average signal decrease of up to $16.2 \pm 2.3\%$ (t -test $P=0.006$, $n=4$) that developed and persisted for over 80 min (Fig. 4f,g), consistent with infiltration of furimazine into the NanoLuc-expressing cell implants and subsequent stimulation of the photosensitive ImpACTs. This mean signal change was $4.5\times$ the amplitude produced by 10^4 cells μ l $^{-1}$ in the in vitro experiment of Supplementary Fig. 9 and therefore suggests that the MRI signal change observed in vivo arose from approximately 5×10^4 cells μ l $^{-1}$ in the sensitive area of the ImpACT.

The MRI change produced by the ImpACT in the vicinity of bioluminescent cells and furimazine injection was significantly different from variations of the MRI signal distal to the ImpACT probes (paired t -test $P=0.02$; $n=4$), which demonstrates that the devices themselves mediated the observed signal changes. MRI scans performed after the experiments showed no evidence of tissue disruption. Furthermore, when the experiments of Fig. 4f,g were repeated with control injections of a fluid lacking furimazine, a statistically insignificant mean MRI intensity increase of $0.4 \pm 1.3\%$ was observed (t -test $P=0.8$; $n=3$; Supplementary Fig. 10). In addition to verifying that the signals documented in Fig. 4f,g arise from bioluminescence detection by the ImpACT devices, the absence of MRI changes in the vehicle control time courses shows that ImpACT devices can perform stably, without a clearly discernible signal drift or biotoxicity, for periods of over 2 h in vivo.

In the experiments of Fig. 4d–g, ImpACT responses to bioluminescent cells in rat brains are slow and monotonic, probably reflecting the combination of diffusive spreading of the furimazine substrate from its infusion site and the relatively constant metabolism of furimazine by NanoLuc-expressing cells. Such time courses are qualitatively consistent with bioluminescence time courses previously observed in vivo⁴⁰ but do not indicate intrinsic temporal limitations of the ImpACT itself. To assess the ability of the device to function on a much faster timescale, we stimulated an implanted device directly with a fibre-optic light source and monitored its response characteristics in vivo (Supplementary Fig. 11). Repeated cycles of light delivery and rest show that the device rapidly cycles between tuned and detuned states with no apparent hysteresis on the timescale of the scan duration. The results also provided an additional testament to the stable performance of ImpACTs in vivo, with no observable attenuation of the light-dependent responses over the 20 min acquisition time investigated. An average MRI signal decrease of $12.7 \pm 0.7\%$ was observed, with a coefficient of variation of about 10% denoting reproducible performance over four stimulation blocks. These measurements therefore collectively demonstrate that ImpACT devices can detect biologically relevant electromagnetic fields reversibly and over a range of timescales in living animals.

Discussion

Our results demonstrate a new principle for the minimally invasive detection of biological signals using biosensitive implantable microdevices that produce localized image changes in MRI. The ImpACT devices accomplish this using simple resonant circuits that require no external power and are detuned by input to a FET. ImpACTs offer several advantages with respect to other implantable device technologies: they are unwired and only interact passively with detection hardware, they do not need to transmit signals out of the body and they can readily be spatially multiplexed in a scalable fashion, in conjunction with MRI-based localization. The ImpACT

design closely parallels that of detunable surface coils for MRI, but on a miniature scale and using components that are sensitive to biologically realistic inputs. In this work we have shown detectability of voltage signals as low as 5.3 mV and luminescent input as low as 1×10^9 ps $^{-1}$. A light-sensitive ImpACT was tested in vivo and it successfully monitored the output of a luciferase gene reporter expressed in a tumour cell model. This was achieved in conjunction with standard MRI hardware, without danger of excessive local energy deposition.

The millimetre-scale devices used in this study could be deployed in many organs of the body where external monitoring of electromagnetic fields is desired. The ImpACT we used for our in vivo experiments had a 3 mm diameter, which is comparable to some electronic implant designs that function by different principles⁴¹. A goal for future development will be to further miniaturize the devices to permit placement using endoscopic procedures or perhaps even infusion into the vasculature. Our theoretical calculations provide a basis for such efforts, showing that ImpACTs with submillimetre diameters are feasible using multi-turn designs (Supplementary Fig. 4). The t_m values of several micrometres required for optimum functionality of such devices can easily be achieved with electroplating techniques that are used for micro-fabricated tethered MRI diagnostics devices^{42,43}. Some studies have demonstrated high-performance microscale coils using wire bonding^{44,45} but this limits scalability due to the serial fabrication process involved. In contrast, our design employs processes that are easy to implement in parallel, thus providing a route for mass production with low manufacturing costs.

Another goal for the future development of ImpACT technology is to expand the scope of potential applications in vivo. For chronic applications in animals or people, this will involve ensuring that the devices are stable and biocompatible over long periods of time. The presented results already demonstrate consistent MRI signal in proximity to ImpACTs over periods of several hours (Supplementary Fig. 10), as well as reproducible, repeated responses to equivalent stimuli across multiple animals (Fig. 4) and multiple cycles of stimulation (Supplementary Fig. 11). Further applications may benefit from passivation strategies that promote tissue compatibility and effective performance of the devices over days, months or years⁴⁶. Expanding the scope of utility may also involve exploring how ImpACT devices could be used in conjunction with diverse magnetic resonance hardware. Although we have shown compatibility of the ImpACTs with MRI-based detection in both conventional clinical and small-bore scanners, multiplexed detection of ImpACTs could be possible using portable systems^{47–49}, albeit with some loss of sensitivity at lower B_0 fields (Supplementary Fig. 7).

When combined with suitable detection hardware, the ImpACTs we have validated here could be used to detect luminescent reporter gene expression in applications such as following tumour growth and treatment in animal models, studying lymphatic function mediated by engineered immune cells or monitoring luciferase-expressing transplanted cells and tissues, potentially in human subjects^{16,50}. For each of these applications, the current light sensitivity of about 1×10^9 ps $^{-1}$ should permit the imaging of cellular events that involve the expression of 10^5 – 10^6 copies of luciferase per cell, assuming an enzyme turnover number of 0.1–1 s $^{-1}$, with as few as 10^4 – 10^5 cells in the vicinity of the $300 \mu\text{m} \times 300 \mu\text{m}$ light-sensitive area of the current device. Integrating ImpACTs with low-dark-current photodiodes would require additional components for more efficient radiofrequency power harvesting by the circuit but could permit detection of as little as 10^6 ps $^{-1}$, enabling sensitivity to luminescent events involving more than an order of magnitude fewer cells or luciferin turnover events. These might, for instance, enable dynamic activity monitoring of calcium-sensitive bioluminescent probes such as aequorin⁵¹, which are estimated to generate fluxes of 1.3×10^3 ps $^{-1}$ per neuron when expressed in vertebrate brains.

The voltage-dependent ImpACT characterized in Fig. 3 displays sensitivity to inputs of 5 mV or more in MRI experiments in vitro and could also be applied for wireless measurements in more or less its present form. The sensitivity of the device is sufficient, in principle, for the dynamic detection of long-range extracellular potentials arising from activated cell populations in neural and muscle tissue. If the device is placed in close apposition to single cells^{52–55}, even individual action potentials could be detectable. The detection of millisecond-timescale transient electrophysiological events is possible provided that those events produce input to the ImpACT during the application of the MRI pulse. As such, the short duration of intracellular and extracellular potentials in electrically active tissue does not present a challenge to their detection using ImpACT technology. Improved sensitivity for the detection of single-cell electrical potentials could be achieved by optimizing FET current–voltage characteristics for more robust detuning of the devices, by potentially using nanowire-based FETs that have been applied in the past for wired electrophysiology measurements²¹.

Another avenue for further development will be the sensitization of ImpACT devices to chemical signals, which can be performed via functionalization of the gate electrode of ion-sensitive FETs with biochemically active agents such as enzymes and antibodies^{33,35,56}. This would enable high specificity ImpACT-based detection of diverse analytes, in proportion to their concentration, via enzymatic or biochemical recognition events that alter the transconductance of the FET. Along with further applications to the detection of electromagnetic fields, the possibility of chemical detection using ImpACTs highlights the versatility of this family of devices for dynamic functional imaging that leverages the spatio-temporal resolution and whole-body volumetric readout capabilities of MRI.

Methods

ImpACT simulations. The performance of ImpACT devices was simulated using equivalent circuit models implemented in PSpice (Cadence Design Systems). The MRI scanner's transmit–receive coil was represented by a resistor–inductor–capacitor circuit assuming a 78 mm diameter ($L = 143.3$ nH), 50 Ohm impedance and a sinusoidal voltage source as coil output. The main coil was inductively coupled to the ImpACT (coupling coefficient $k = 0.00275–0.275$), which was represented by another resistor–inductor–capacitor circuit that was connected in parallel to an FET component. The ImpACT inductance ranged from 0.2 to 32 nH and the capacitance ranged from 4.8 to 791.7 pF. The resistance was calculated based on sheet resistance considerations and skin depth at 400 MHz. The sensitivity profiles of the modelled FET devices simulated here were based on product descriptions of the 2N5486 metal oxide semiconductor FET (MOSFET) from Central Semiconductor Corp. and the SFH3310 photoFET from Osram Opto Semiconductors.

Current output from the model was converted to B_{ImpACT} by using the Biot–Savart law for magnetic field produced by a current loop and the ratio between B_{ImpACT} and the B_1 of the main coil was used as an estimate of MRI signal amplification due to the device. The justification for this approach is that, for a wide family of MRI pulse protocols, including the gradient echo methods used in this paper, the MRI signal amplitude detected is proportional to $\sin(\alpha)$, where α is the flip angle of the excitation pulse. Given that α is in turn directly proportional to the local radiofrequency field during the excitation pulse, the local amplification of this field (as reflected by B_{ImpACT}/B_1) will also determine the local amplification of the MRI signal. This analysis applies to low flip angles, significantly smaller than 90°, as typically used in longitudinal relaxation time (T_1)-weighted imaging. For larger flip angles, the relationship between local B_1 enhancement and the resulting MRI signal will be more complex but may nevertheless be analytically derived. Note that this analysis ignores the potential effect of ImpACT detuning on signal reception during the acquisition phase of the MRI pulse sequence; this effect is harder to model but, if present, would synergize with effects due to ImpACT tuning during pulse generation. For the two-dimensional plots of Fig. 2 and Supplementary Figs. 1 and 2, we evaluated 55 input values between 0 and 500 mV (0 and 10^{10} p s⁻¹) spaced linearly according to the equivalent FET channel conductivity, 18 diameter values spaced logarithmically between 10 and 5000 μm and 10 t_m values spaced linearly between 1 and 10 μs . The $\Delta(B_{\text{ImpACT}}/B_1)$ values presented in Supplementary Figs. 1 and 2 were determined as the B_{ImpACT}/B_1 for the parameters indicated by the axes minus the B_{ImpACT}/B_1 for zero input.

Calculation of power dissipation. We estimated an upper bound on the maximum local SAR of an ImpACT by calculating the maximum instantaneous power (P) deposited in the ImpACT during an radiofrequency pulse and normalizing this

by a spherical volume of tissue (V) around the device, with twice the diameter of the device. This volume was chosen conservatively to reflect the maximal density at which multiple functional ImpACT devices could be spaced in tissue, with a separation of twice their diameter thus minimizing the potential for electromagnetic coupling between the devices; in most applications, the inter-device spacing and corresponding volumes of power dissipation are likely to be much greater. Under the simulation conditions, we calculate:

$$\frac{P}{V} = \frac{\rho I_{\text{ImpACT}}^2 R_{\text{ImpACT}}}{4/3\pi d^3} \quad (1)$$

where ρ is the tissue density (approximately 1 kg l^{-3}), R_{ImpACT} is the device impedance at 400 MHz and I_{ImpACT} is the current induced in the device, computed using the B_{ImpACT}/B_1 ratios of Fig. 2c and assuming an applied radiofrequency field of $2 \mu\text{T}$. The value of $2 \mu\text{T}$ for the scanner's radiofrequency pulse amplitude is chosen by assuming a pulse width (t_p) of 1 ms and alpha of 30°, using the formula

$$B_1 = \frac{\alpha}{\gamma t_p} \quad (2)$$

with proton gyromagnetic ratio γ of 42.6 MHz T⁻¹. The P/V values computed using equation 1 and presented in Supplementary Fig. 5 are likely to be substantial overestimates of the actual SAR, for three reasons: (1) the sparse duty cycle of pulsing in a typical MRI experiment (usually less than 1%); (2) only a fraction of the power dissipated in the ImpACT is actually likely to be transferred into the tissue as heat and (3) as noted above, the tissue volume over which power can be spread will probably be significantly larger than twice the device diameter.

Device fabrication and characterization. Circuits were fabricated using standard printed-circuit single-turn inductors with 10 μm gold-plated copper as a conductive layer. The coil radius ranged from 500 μm to 5 mm with line width of 0.1–1 mm. Coils were soldered to trimmer capacitors with adjustable capacitance of 5.5–30 pF (Knowles Voltronics #JR300). For voltage measurements, we used N-Channel 400 MHz radiofrequency MOSFETs with internal capacitance of 5 pF (Central Semiconductor Corp. #2N5486). For MRI photodetection and bioluminescence measurements, we used NPN phototransistors with 570 nm wavelength peak sensitivity and collector emitter capacitance of 2.2–4.0 pF (Osram Opto Semiconductors #SFH3310). The photon-sensitive area of these components was 300 $\mu\text{m} \times 300 \mu\text{m}$. For bioluminescence measurements outside of the MRI scanner, we used the IVIS Spectrum in vivo imaging system (PerkinElmer). Current measurements were made using a custom-made amperometer circuit and 10 GHz oscilloscope (Keysight Technologies #DSO81004B). Resonance frequency characterization was performed using a radiofrequency network analyser (Keysight Technologies, #E5061A) by way of reflected amplitude measurements using a loop antenna comprised of 2 mm copper-shielded coaxial silver wire (Pasternack #RG402-U), placed 0.5 mm above the ImpACT inductor. For water phantom measurements, 0.5 ml microcentrifuge tubes were cut and cured on top of the ImpACT coils using epoxy glue. Temperature measurements were performed using SurgiVET Advisor monitor and V3417 temperature probe (Smiths Medical).

MRI validation and data analysis. Magnetic resonance imaging was performed primarily using a 9.4T Avance II MRI scanner (Bruker Instruments). Additional measurements at clinical field were performed using a Siemens 3T MAGNETOM Tim Trio scanner. ImpACT devices were cured to polymer tubes for measurement in solution and placed within a birdcage transmit–receive imaging volume coil (78 mm inner diameter). The response to light intensity was measured in light-tight chambers. Both T_1 -weighted scans and transverse relaxation time (T_2)-weighted scans with 0.1–1 mm slice thickness across the surface of the devices were acquired using gradient echo and fast spin echo-pulse sequences. Echo time (TE) of 15.6 ms and repetition times (TR) of 250 and 787 ms were used. Data matrices of 64×64 , 128×128 and 256×256 points were taken, with 1–10 averages and total scan time ranging between 16 s and 10 min. Intensity values in square regions of interest at the centre of the device surface were determined from reconstructed magnitude images and compared to baseline values from regions distal to the device. Analysis was performed using custom routines written in MATLAB. Time-lapse scans for functional imaging were obtained using a gradient echo-pulse sequence with a flip angle of 30°, TR of 236 ms, TE of 15.6 ms, field of view of 25.6 mm \times 25.6 mm, data matrix of 128×128 points and 1 mm coronal slice thickness, with 16 s scan time. Scans were obtained consecutively for 1 h. The post-processing of MRI data was performed using customized routines in MATLAB (Mathworks). Raw images were analysed per region of interest around inductor element of device for the quantification of signal amplitude before and after detuning.

Cellular expression of luciferase. Phantom measurements were taken at room temperature using either deionized water or PBS (pH 7.4). Magnetic resonance imaging of biological luminescence was performed in PBS, using recombinant luciferase from *Photinus pyralis* (Sigma Aldrich) at a concentration of 7.8 μM and an initial volume of 100 μl . D-luciferin (Sigma Aldrich) at a concentration of 7.8 mM in argon-bubbled deionized water and equimolar concentration of sodium bicarbonate, and adenosine 5'-triphosphate (ATP) disodium salt hydrate

(Sigma Aldrich) at a concentration of 7.8 mM, were each dissolved in a volume of 50 μ l and were both mixed with luciferase solution during MRI to achieve a working concentration of 3.9 μ M of luciferase and 3.9 mM of luciferin and ATP. For bioluminescence cell measurements, we used a HEK293 cell line transfected with NanoLuc-engineered luciferase plasmid (Promega). Bioluminescence was measured 48 h after transfection by adding 1–5 mM furimazine (Promega) to 10×10^6 cells ml^{-1} in Tris buffer at the phototransistor component of device.

Animal use. Male Sprague-Dawley rats (250–300 g) were purchased from Charles River Laboratories and used for all in vivo experiments. The animals were housed and maintained on a 12 h light/dark cycle and permitted ad libitum access to food and water. All procedures were performed in strict compliance with US Federal guidelines, with oversight by the MIT Committee on Animal Care.

MRI detection of luciferase-expressing cells in vivo. Intracerebral guide cannulae were implanted surgically to facilitate intracranial injection of furimazine in MRI experiments, emulating previously described methods⁵⁷. The animals were anaesthetized with isoflurane (4% induction, 2% maintenance), shaved and mounted on a rodent stereotaxic device (Kopf Instruments) with heating pad. Heart rates and blood oxygenation were continuously monitored using a pulse oximeter (Nonin Medical) during all subsequent procedures. The scalp was retracted and two small holes were drilled into the skull, 7 mm and 9 mm posterior to bregma and 0.5 mm lateral to the midline. An MRI-compatible 2-mm-long guide cannula (22 gauge; PlasticsOne) was implanted at the anterior site. A NanoLuc-expressing HEK293 cell slurry (10 μ l containing $\sim 5 \times 10^6$ cells) was injected into the cortex at the posterior site and an ImpACT device was implanted over the cells. A custom-fabricated plastic headpost was attached to the skull in front of the guide cannula and dental cement was applied to secure all implants rigidly in place. Buprenorphin (0.05 mg kg^{-1}) was injected subcutaneously during surgery. An MRI-compatible injection cannula (3 mm long below pedestal; PlasticsOne) was connected to microtubing pre-filled with 5 μ l 7.8 μ M furimazine. The injection cannula was slowly lowered into the previously implanted guide cannula while infusing furimazine at a low injection rate to prevent air from becoming trapped during insertion. The injection cannula was then secured to the guide cannula with dental cement and the injection was paused.

Each animal was then transferred to a plexiglass cradle covered with a water heating blanket to maintain body temperature and inserted into a transmit–receive volume coil (Bruker Instruments). The animal was positioned at the isocentre of a 9.4 T Bruker Avance II scanner (Bruker Instruments). The heart rate and oxygen saturation levels were monitored throughout the scan using a Nonin 8600 V pulse oximeter (Nonin Medical) and breathing and expired CO_2 were monitored using a SurgiVet V9004 Capnograph. Heart rates were maintained at 360–380 beats per minute. A continuous flow of 1.5% isoflurane was delivered to the animals for the duration of the scanning sessions.

For in vivo MRI analysis, T_1 -weighted scan series and T_2 -weighted anatomical scans were obtained from each animal. Multislice anatomical images with 200 μ m in-plane resolution over six 1 mm sagittal slices were obtained using a rapid acquisition with relaxation enhancement (RARE) pulse sequence with a TR of 2 s, TE of 14 ms, RARE factor of 8, field of view of 25.6 mm \times 25.6 mm, data matrix of 128 \times 128 points, 4 averages and a total scan time of 80 s. Scan series for functional imaging were obtained using a gradient echo-pulse sequence with a flip angle of 30°, TR of 126 ms, TE of 10 ms, field of view of 25.6 mm \times 25.6 mm, data matrix of 128 \times 128 points and 1 mm sagittal slice thickness with 16 s scan time per image. Scans were obtained consecutively for 2 h; from $t = 5$ to 35 min, furimazine was infused at a constant rate of 0.1 μ l min^{-1} .

Reporting Summary. Further information on research design is available in the Nature Research Reporting Summary linked to this article.

Code availability. The MATLAB code for the simulation of the MRI response and of the design parameters of ImpACT devices is available from the corresponding author on reasonable request.

Data availability

The data that support the findings of this study are available within the paper and its Supplementary Information. All datasets generated for this study are available from the corresponding author on reasonable request.

Received: 6 December 2017; Accepted: 6 September 2018;

Published online: 22 October 2018

References

- Grosse, P., Cassidy, M. J. & Brown, P. EEG-EMG, MEG-EMG and EMG-EMG frequency analysis: physiological principles and clinical applications. *Clin. Neurophysiol.* **113**, 1523–1531 (2002).
- Jasanoff, A. Bloodless fMRI. *Trends Neurosci.* **30**, 603–610 (2007).
- Logothetis, N. K. What we can do and what we cannot do with fMRI. *Nature* **453**, 869 (2008).
- Bandettini, P. A. What's new in neuroimaging methods? *Ann. NY Acad. Sci.* **1156**, 260–293 (2009).
- Regan, D. *Human Brain Electrophysiology: Evoked Potentials and Evoked Magnetic Fields in Science and Medicine* (Elsevier, New York, 1989).
- Merletti, R. & Parker, P. A. *Electromyography: Physiology, Engineering, and Non-Invasive Applications* Vol. 11 (John Wiley & Sons, Hoboken, 2004).
- Nunez, P. L. & Srinivasan, R. *Electric Fields of the Brain: The Neurophysics of EEG* (Oxford Univ. Press, New York, 2006).
- Bénar, C. et al. Quality of EEG in simultaneous EEG-fMRI for epilepsy. *Clin. Neurophysiol.* **114**, 569–580 (2003).
- Pandarínath, C. et al. Neural population dynamics in human motor cortex during movements in people with ALS. *eLife* **4**, e07436 (2015).
- Cash, S. S. & Hochberg, L. R. The emergence of single neurons in clinical neurology. *Neuron* **86**, 79–91 (2015).
- Wang, J. Amperometric biosensors for clinical and therapeutic drug monitoring: a review. *J. Pharm. Biomed. Anal.* **19**, 47–53 (1999).
- Wang, J. Electrochemical biosensors: towards point-of-care cancer diagnostics. *Biosens. Bioelectron.* **21**, 1887–1892 (2006).
- Sofic, E., Lange, K. W., Jellinger, K. & Riederer, P. Reduced and oxidized glutathione in the substantia nigra of patients with Parkinson's disease. *Neurosci. Lett.* **142**, 128–130 (1992).
- Bergamini, M. F., Santos, A. L., Stradiotto, N. R. & Zanoni, M. V. A disposable electrochemical sensor for the rapid determination of levodopa. *J. Pharm. Biomed. Anal.* **39**, 54–59 (2005).
- Wassum, K. M. et al. Silicon wafer-based platinum microelectrode array biosensor for near real-time measurement of glutamate in vivo. *Sensors* **8**, 5023–5036 (2008).
- Contag, C. H. & Bachmann, M. H. Advances in in vivo bioluminescence imaging of gene expression. *Annu. Rev. Biomed. Eng.* **4**, 235–260 (2002).
- Weissleder, R. & Ntziachristos, V. Shedding light onto live molecular targets. *Nat. Med.* **9**, 123–128 (2003).
- Lee, A. K., Manns, I. D., Sakmann, B. & Brecht, M. Whole-cell recordings in freely moving rats. *Neuron* **51**, 399–407 (2006).
- Kodandaramaiah, S. B., Franzesi, G. T., Chow, B. Y., Boyden, E. S. & Forest, C. R. Automated whole-cell patch-clamp electrophysiology of neurons in vivo. *Nat. Methods* **9**, 585–587 (2012).
- Hochberg, L. R. et al. Neuronal ensemble control of prosthetic devices by a human with tetraplegia. *Nature* **442**, 164–171 (2006).
- Spira, M. E. & Hai, A. Multi-electrode array technologies for neuroscience and cardiology. *Nat. Nanotech.* **8**, 83–94 (2013).
- Stosiek, C., Garaschuk, O., Holthoff, K. & Konnerth, A. In vivo two-photon calcium imaging of neuronal networks. *Proc. Natl Acad. Sci. USA* **100**, 7319–7324 (2003).
- Flusberg, B. A. et al. Fiber-optic fluorescence imaging. *Nat. Methods* **2**, 941–950 (2005).
- Seo, D., Carmena, J. M., Rabaey, J. M., Maharbiz, M. M. & Alon, E. Model validation of untethered, ultrasonic neural dust motes for cortical recording. *J. Neurosci. Methods* **244**, 114–122 (2015).
- Seo, D. et al. Wireless recording in the peripheral nervous system with ultrasonic neural dust. *Neuron* **91**, 529–539 (2016).
- Frank, S. & Lauterbur, P. C. Voltage-sensitive magnetic gels as magnetic resonance monitoring agents. *Nature* **363**, 334–336 (1993).
- Kruttwig, K. et al. Reversible low-light induced photoswitching of crowned spiropyran-DO3A complexed with gadolinium (III) ions. *Molecules* **17**, 6605–6624 (2012).
- Louie, A. Multimodality imaging probes: design and challenges. *Chem. Rev.* **110**, 3146–3195 (2010).
- Weis, R., Müller, B. & Fromherz, P. Neuron adhesion on a silicon chip probed by an array of field-effect transistors. *Phys. Rev. Lett.* **76**, 327–330 (1996).
- Cohen, A. et al. Depletion type floating gate p-channel MOS transistor for recording action potentials generated by cultured neurons. *Biosens. Bioelectron.* **19**, 1703–1709 (2004).
- Lorach, H. et al. Photovoltaic restoration of sight with high visual acuity. *Nat. Med.* **21**, 476–482 (2015).
- Palanker, D., Vankov, A., Huie, P. & Baccus, S. Design of a high-resolution optoelectronic retinal prosthesis. *J. Neural Eng.* **2**, S105–S120 (2005).
- Luo, X.-L., Xu, J.-J., Zhao, W. & Chen, H.-Y. Glucose biosensor based on ENFET doped with SiO_2 nanoparticles. *Sens. Actuators B* **97**, 249–255 (2004).
- Miyahara, Y., Moriizumi, T. & Ichimura, K. Integrated enzyme FETs for simultaneous detections of urea and glucose. *Sens. Actuators* **7**, 1–10 (1985).
- Hai, A. et al. Acetylcholinesterase-ISFET based system for the detection of acetylcholine and acetylcholinesterase inhibitors. *Biosens. Bioelectron.* **22**, 605–612 (2006).
- Lyons, S. K. et al. Noninvasive bioluminescence imaging of normal and spontaneously transformed prostate tissue in mice. *Cancer Res.* **66**, 4701–4707 (2006).
- Evans, M. S. et al. A synthetic luciferin improves bioluminescence imaging in live mice. *Nat. Methods* **11**, 393–395 (2014).

38. Juchem, C. & de Graaf, R. A. B. magnetic field homogeneity and shimming for in vivo magnetic resonance spectroscopy. *Anal. Biochem.* **529**, 17–29 (2017).
39. Center for Devices and Radiological Health *Criteria for Significant Risk Investigations of Magnetic Resonance Diagnostic Devices* (US Food and Drug Administration, 2014).
40. Iwano, S. et al. Single-cell bioluminescence imaging of deep tissue in freely moving animals. *Science* **359**, 935–939 (2018).
41. Ho, J. S. et al. Wireless power transfer to deep-tissue microimplants. *Proc. Natl Acad. Sci. USA* **111**, 7974–7979 (2014).
42. Lee, H., Sun, E., Ham, D. & Weissleder, R. Chip-NMR biosensor for detection and molecular analysis of cells. *Nat. Med.* **14**, 869–874 (2008).
43. Haun, J. B. et al. Micro-NMR for rapid molecular analysis of human tumor samples. *Sci. Transl. Med.* **3**, 71ra16 (2011).
44. Kratt, K., Badilita, V., Burger, T., Korvink, J. & Wallrabe, U. A fully MEMS-compatible process for 3D high aspect ratio micro coils obtained with an automatic wire bonder. *J. Micromech. Microeng.* **20**, 015021 (2009).
45. Fischer, A. C. et al. Unconventional applications of wire bonding create opportunities for microsystem integration. *J. Micromech. Microeng.* **23**, 083001 (2013).
46. Feiner, R. & Dvir, T. Tissue–electronics interfaces: from implantable devices to engineered tissues. *Nat. Rev. Mater.* **3**, 17076 (2017).
47. Eidmann, G., Savelsberg, R., Blümler, P. & Blümich, B. The NMR MOUSE, a mobile universal surface explorer. *J. Magn. Reson.* **122**, 104–109 (1996).
48. Demas, V. et al. Three-dimensional phase-encoded chemical shift MRI in the presence of inhomogeneous fields. *Proc. Natl Acad. Sci. USA* **101**, 8845–8847 (2004).
49. Cooley, C. Z. et al. Design of sparse Halbach magnet arrays for portable MRI using a genetic algorithm. *IEEE Trans. Magn.* **54**, 1–12 (2018).
50. Negrin, R. S. & Contag, C. H. In vivo imaging using bioluminescence: a tool for probing graft-versus-host disease. *Nat. Rev. Immunol.* **6**, 484–490 (2006).
51. Naumann, E. A., Kampff, A. R., Prober, D. A., Schier, A. F. & Engert, F. Monitoring neural activity with bioluminescence during natural behavior. *Nat. Neurosci.* **13**, 513–520 (2010).
52. Hai, A. et al. Changing gears from chemical adhesion of cells to flat substrata toward engulfment of micro-protrusions by active mechanisms. *J. Neural Eng.* **6**, 066009 (2009).
53. Hai, A. et al. Spine-shaped gold protrusions improve the adherence and electrical coupling of neurons with the surface of micro-electronic devices. *J. R. Soc. Interface.* **6**, 1153–1165 (2009).
54. Hai, A., Shappir, J. & Spira, M. E. In-cell recordings by extracellular microelectrodes. *Nat. Methods* **7**, 200–202 (2010).
55. Hai, A., Shappir, J. & Spira, M. E. Long-term, multisite, parallel, in-cell recording and stimulation by an array of extracellular microelectrodes. *J. Neurophysiol.* **104**, 559–568 (2010).
56. Katz, E. & Willner, I. Probing biomolecular interactions at conductive and semiconductive surfaces by impedance spectroscopy: routes to impedimetric immunosensors, DNA-sensors, and enzyme biosensors. *Electroanalysis* **15**, 913–947 (2003).
57. Hai, A., Cai, L. X., Lee, T., Lelyveld, V. S. & Jasanoff, A. Molecular fMRI of serotonin transport. *Neuron* **92**, 754–765 (2016).

Acknowledgements

This research was funded by NIH grants R01 NS76462, R01 DA038642 and U01 NS904051 to A.J. A.H. was supported by postdoctoral fellowships from the Edmond & Lily Safra Center for Brain Sciences and a long-term fellowship of the European Molecular Biology Organization. We thank A. Takahashi for assistance with 3 T MRI measurements.

Author contributions

A.H. and A.J. devised the ImpACT concept. A.H., V.C.S., B.B.B. and A.J. designed the research. A.H. performed the modelling calculations. A.H. and V.C.S. performed the in vitro measurements and analysed the data. A.H. and B.B.B. performed the in vivo imaging experiments. A.H. and A.J. wrote the manuscript.

Competing interests

MIT has filed a provisional patent application related to this technology.

Additional information

Supplementary information is available for this paper at <https://doi.org/10.1038/s41551-018-0309-8>.

Reprints and permissions information is available at www.nature.com/reprints.

Correspondence and requests for materials should be addressed to A.J.

Publisher's note: Springer Nature remains neutral with regard to jurisdictional claims in published maps and institutional affiliations.

© The Author(s), under exclusive licence to Springer Nature Limited 2018

Life Sciences Reporting Summary

Nature Research wishes to improve the reproducibility of the work that we publish. This form is intended for publication with all accepted life science papers and provides structure for consistency and transparency in reporting. Every life science submission will use this form; some list items might not apply to an individual manuscript, but all fields must be completed for clarity.

For further information on the points included in this form, see [Reporting Life Sciences Research](#). For further information on Nature Research policies, including our [data availability policy](#), see [Authors & Referees](#) and the [Editorial Policy Checklist](#).

Please do not complete any field with "not applicable" or n/a. Refer to the help text for what text to use if an item is not relevant to your study. For final submission: please carefully check your responses for accuracy; you will not be able to make changes later.

▶ Experimental design

1. Sample size

Describe how sample size was determined.

The experiments reported replicated tests of individual devices. Very high signal-to-noise measurements were possible, and predetermination of sample size was unnecessary.

2. Data exclusions

Describe any data exclusions.

No data were excluded from the analysis.

3. Replication

Describe the measures taken to verify the reproducibility of the experimental findings.

All replications of measurements were successful.

4. Randomization

Describe how samples/organisms/participants were allocated into experimental groups.

In vivo MRI measurements of bioluminescent cell lines were performed in two groups of four animals for replication and control purposes, respectively, in order to test device performance. Different brain regions within each animal were compared (proximal/distal to device).

5. Blinding

Describe whether the investigators were blinded to group allocation during data collection and/or analysis.

Blinding was not relevant.

Note: all in vivo studies must report how sample size was determined and whether blinding and randomization were used.

6. Statistical parameters

For all figures and tables that use statistical methods, confirm that the following items are present in relevant figure legends (or in the Methods section if additional space is needed).

- | n/a | Confirmed |
|--------------------------|--|
| <input type="checkbox"/> | <input checked="" type="checkbox"/> The <u>exact sample size</u> (<i>n</i>) for each experimental group/condition, given as a discrete number and unit of measurement (animals, litters, cultures, etc.) |
| <input type="checkbox"/> | <input checked="" type="checkbox"/> A description of how samples were collected, noting whether measurements were taken from distinct samples or whether the same sample was measured repeatedly |
| <input type="checkbox"/> | <input checked="" type="checkbox"/> A statement indicating how many times each experiment was replicated |
| <input type="checkbox"/> | <input checked="" type="checkbox"/> The statistical test(s) used and whether they are one- or two-sided
<i>Only common tests should be described solely by name; describe more complex techniques in the Methods section.</i> |
| <input type="checkbox"/> | <input checked="" type="checkbox"/> A description of any assumptions or corrections, such as an adjustment for multiple comparisons |
| <input type="checkbox"/> | <input checked="" type="checkbox"/> Test values indicating whether an effect is present
<i>Provide confidence intervals or give results of significance tests (e.g. P values) as exact values whenever appropriate and with effect sizes noted.</i> |
| <input type="checkbox"/> | <input checked="" type="checkbox"/> A clear description of statistics including <u>central tendency</u> (e.g. median, mean) and <u>variation</u> (e.g. standard deviation, interquartile range) |
| <input type="checkbox"/> | <input checked="" type="checkbox"/> Clearly defined error bars in <u>all</u> relevant figure captions (with explicit mention of central tendency and variation) |

See the web collection on [statistics for biologists](#) for further resources and guidance.

► Software

Policy information about [availability of computer code](#)

7. Software

Describe the software used to analyze the data in this study.

MATLAB (Mathworks, Natick, MA).

For manuscripts utilizing custom algorithms or software that are central to the paper but not yet described in the published literature, software must be made available to editors and reviewers upon request. We strongly encourage code deposition in a community repository (e.g. GitHub). *Nature Methods* [guidance for providing algorithms and software for publication](#) provides further information on this topic.

► Materials and reagents

Policy information about [availability of materials](#)

8. Materials availability

Indicate whether there are restrictions on availability of unique materials or if these materials are only available for distribution by a third party.

No known restrictions.

9. Antibodies

Describe the antibodies used and how they were validated for use in the system under study (i.e. assay and species).

No antibodies were used.

10. Eukaryotic cell lines

a. State the source of each eukaryotic cell line used.

ThermoFisher (FreeStyle 293 cells).

b. Describe the method of cell line authentication used.

Cells were obtained directly from the supplier, and additional authentication was not performed.

c. Report whether the cell lines were tested for mycoplasma contamination.

Not explicitly, but bioluminescence indicated cell viability and performance.

d. If any of the cell lines used are listed in the database of commonly misidentified cell lines maintained by [ICLAC](#), provide a scientific rationale for their use.

No commonly misidentified cell lines were used.

► Animals and human research participants

Policy information about [studies involving animals](#); when reporting animal research, follow the [ARRIVE guidelines](#)

11. Description of research animals

Provide all relevant details on animals and/or animal-derived materials used in the study.

Male Sprague-Dawley rats (250–300 g) were purchased from Charles River Laboratories (Wilmington, MA) and used for all in vivo experiments.

Policy information about [studies involving human research participants](#)

12. Description of human research participants

Describe the covariate-relevant population characteristics of the human research participants.

The study did not involve human research participants.

MRI Studies Reporting Summary

Form fields will expand as needed. Please do not leave fields blank.

▶ Experimental design

1. Describe the experimental design.
2. Specify the number of blocks, trials or experimental units per session and/or subject, and specify the length of each trial or block (if trials are blocked) and interval between trials.
3. Describe how behavioral performance was measured.

▶ Acquisition

4. Imaging
 - a. Specify the type(s) of imaging.
 - b. Specify the field strength (in Tesla).
 - c. Provide the essential sequence imaging parameters.
 - d. For diffusion MRI, provide full details of imaging parameters.
5. State area of acquisition.

▶ Preprocessing

6. Describe the software used for preprocessing.
7. Normalization
 - a. If data were normalized/standardized, describe the approach(es).
 - b. Describe the template used for normalization/transformation.
8. Describe your procedure for artifact and structured noise removal.
9. Define your software and/or method and criteria for volume censoring, and state the extent of such censoring.

► Statistical modeling & inference

10. Define your model type and settings.

No statistical modeling or inference was used in this study.

11. Specify the precise effect tested.

Experiments tested for signal changes over time.

12. Analysis

a. Specify whether analysis is whole brain or ROI-based.

Both voxel-level and ROI-based measures are presented in Fig. 4 and Supplementary Figs. 10 and 11.

b. If ROI-based, describe how anatomical locations were determined.

ROI was aligned with the position of the device being tested.

13. State the statistic type for inference.
(See [Eklund et al. 2016](#).)

No statistical modeling or inference was used in this study.

14. Describe the type of correction and how it is obtained for multiple comparisons.

Corrections for multiple comparisons were not relevant.

15. Connectivity

a. For functional and/or effective connectivity, report the measures of dependence used and the model details.

No connectivity analysis was performed.

b. For graph analysis, report the dependent variable and functional connectivity measure.

No connectivity analysis was performed.

16. For multivariate modeling and predictive analysis, specify independent variables, features extraction and dimension reduction, model, training and evaluation metrics.

These analyses were not used.

In the format provided by the authors and unedited.

Wireless resonant circuits for the minimally invasive sensing of biophysical processes in magnetic resonance imaging

Aviad Hai ¹, Virginia Ch. Spanoudaki², Benjamin B. Bartelle¹ and Alan Jasanoff ^{1,3,4*}

¹Department of Biological Engineering, Massachusetts Institute of Technology, Cambridge, MA, USA. ²Koch Institute for Integrative Cancer Research, Massachusetts Institute of Technology, Cambridge, MA, USA. ³Department of Brain and Cognitive Sciences, Massachusetts Institute of Technology, Cambridge, MA, USA. ⁴Department of Nuclear Science and Engineering, Massachusetts Institute of Technology, Cambridge, MA, USA.

*e-mail: jasanoff@mit.edu

SUPPLEMENTARY INFORMATION

Table of Contents	page
Supplementary Text	2
Supplementary Figure 1. Change in enhancement of local RF field intensity as a function of ImpACT dimensions and input strength	3
Supplementary Figure 2. Enhancement of local RF intensity as a function of film thickness and input strength	4
Supplementary Figure 3. ImpACT sensitivity as a function of FET transconductance	5
Supplementary Figure 4. Sensitivity of submillimeter multiturn ImpACT devices to voltaic and photonic inputs	6
Supplementary Figure 5. Sensitivity of ImpACTs to biologically relevant fields	7
Supplementary Figure 6. ImpACT sensitivity to environmental changes	8
Supplementary Figure 7. ImpACT sensitivity at different MRI field strengths	9
Supplementary Figure 8. Maximum local specific power dissipation by ImpACT devices	10
Supplementary Figure 9. Time course of relative MRI signal produced by NanoLuc-expressing cells	11
Supplementary Figure 10. MRI monitoring of ImpACT response to sham injections of saline in live rat brains	12
Supplementary Figure 11. Reversible detuning of an ImpACT device in live rat brain	13

SUPPLEMENTARY TEXT

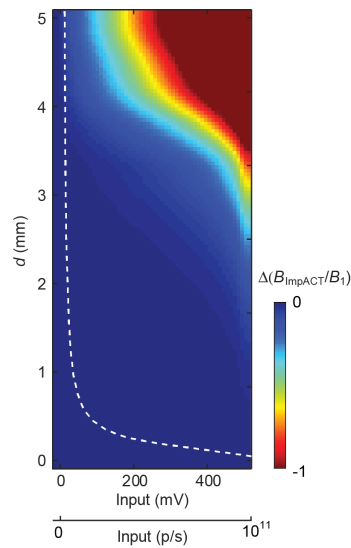
Additional ImpACT design considerations

To evaluate the ImpACT circuit metal layer thickness (t_m) required for sensing electrical or photonic input, we simulated the response of devices with feasible t_m values ranging between 500 nm and 10 μm . Throughout most of this range, reducing t_m increases the impedance of its inductor component, lowering the device's Q and reducing the coupling efficiency between the ImpACT and the MRI coil. **Supplementary Fig. 2** shows that this has the effect of reducing the change in B_{ImpACT}/B_1 that can be achieved by modulating inputs to the device, lowering its sensitivity. For devices with t_m greater than 8 μm (thicker than twice the skin depth at 400 MHz), performance is approximately constant, with inputs producing up to 63% changes in B_{ImpACT}/B_1 . For $t_m < 1 \mu\text{m}$, no discernable change in B_{ImpACT}/B_1 can be produced however.

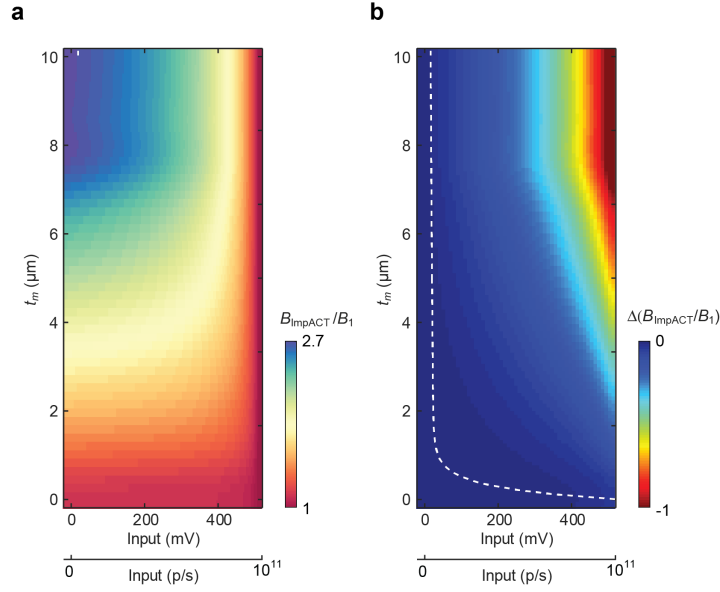
Although the simulated data of **Fig. 2** and **Supplementary Fig. 2** establish lower bounds of $d = 1 \text{ mm}$ and $t_m = 1 \mu\text{m}$ on the fabrication of sensitive ImpACT devices produced with single turn inductors and commercially available compact FETs, we examined additional design factors that could permit improved sensitivity or further miniaturization of the devices in future work. **Supplementary Fig. 3** shows that one route to achieving improved sensitivity is to increase the FET or photoFET's transconductance (g_m), defined as the reciprocal of its drain-source resistance in the fully open state. By increasing g_m four-fold from the value of 5×10^{-3} used in the simulations of **Fig. 2**, the predicted response of a 1 mm ImpACT to a 10 mV input increases by 79%, and the minimum detectable input reaches 11.3 mV or 2.3×10^9 p/s.

A second strategy for improving sensitivity involves increasing the number of turns of the ImpACT inductor coil. **Supplementary Fig. 4** shows that devices with diameters 1 mm, 500 μm , 250 μm , and 100 μm , can achieve 1% changes in B_{ImpACT}/B_1 in response to inputs of 5.6 mV, 5.8 mV, 9.9 mV, and 33 mV respectively.

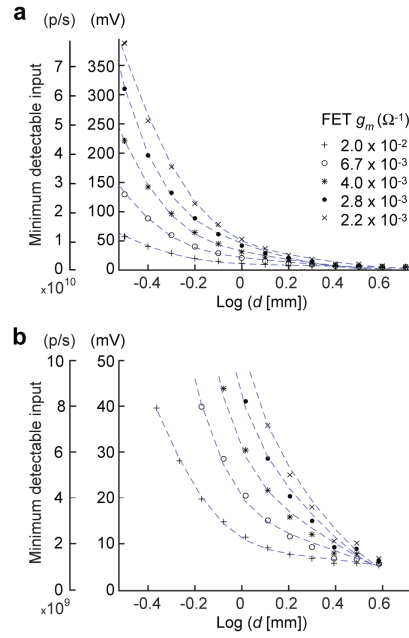
SUPPLEMENTARY FIGURES



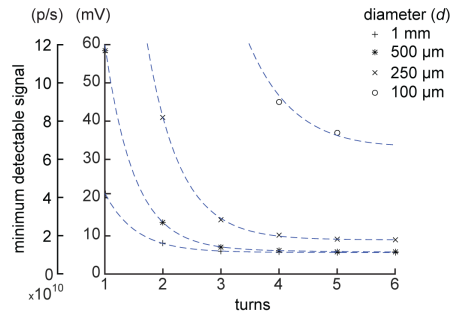
Supplementary Figure 1. Change in enhancement of local RF field intensity as a function of ImpACT dimensions and input strength. MRI effects are modeled as enhancements to the local RF field in the neighborhood of the ImpACT device (B_{ImpACT}/B_1). This graph shows the change in B_{ImpACT}/B_1 at each input amplitude (mV or p/s), with respect to zero input, for each value of the device diameter (d). The white dashed line denotes minimum inputs required to produce 1% change in B_{ImpACT}/B_1 , with respect to zero input, for each value of d .



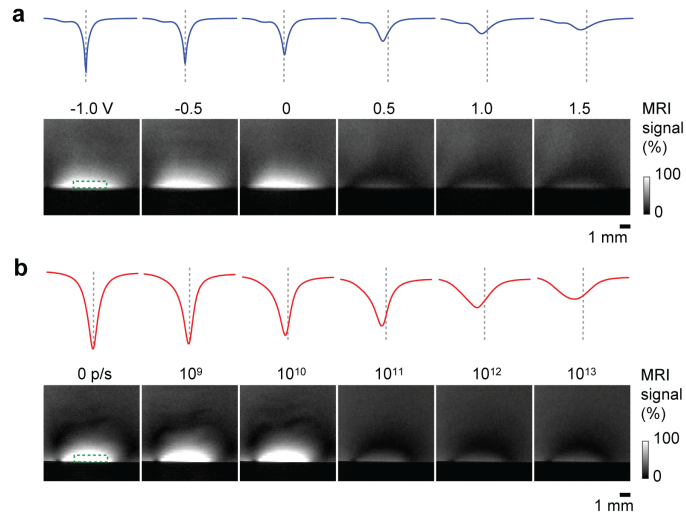
Supplementary Figure 2. Enhancement of local RF intensity as a function of film thickness and input strength. (a) MRI effects are modeled as enhancements to the local RF field in the neighborhood of the device (B_{ImpACT}/B_1), as a function of the ImpACT film thickness (t_m) and the gate input strength in mV or p/s, assuming a device diameter of $d = 3$ mm. For $t_m < 8 \mu\text{m}$, the difference between MRI signal in the low vs. high input states decreases rapidly, and for $t_m < 1 \mu\text{m}$ falls below the estimated detection limit of 1% change in B_{ImpACT}/B_1 for the entire input range. This sets a lower bound on t_m necessary for constructing effective ImpACT sensors. **(b)** The same results shown as the change in B_{ImpACT}/B_1 at each input amplitude, with respect to zero input, for each value of t_m . The white dashed line denotes minimum inputs required to produce 1% change in B_{ImpACT}/B_1 , with respect to zero input, for each value of t_m .



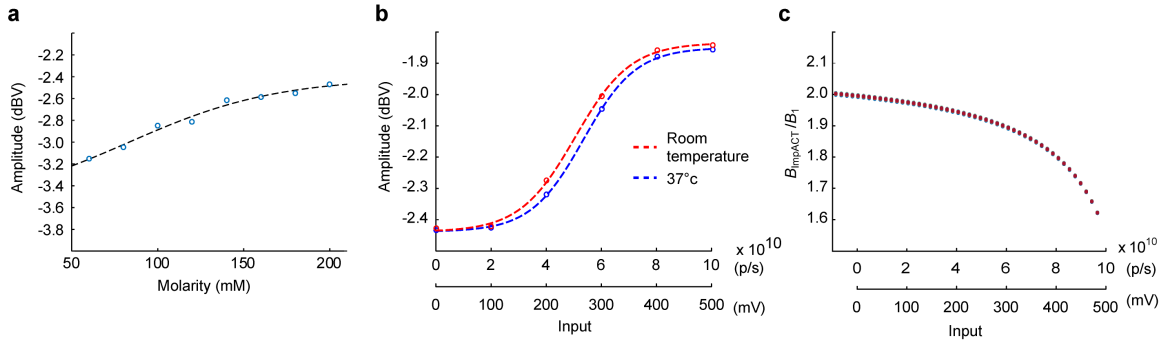
Supplementary Figure 3. ImpACT sensitivity as a function of FET transconductance. Minimum photonic and voltaic input signals predicted to produce 1% change or greater in B_{ImpACT}/B_1 were computed as a function of device diameter (d) for various transconductance (g_m) values shown. Panel (a) shows the full range of sensitivities for devices of $d = 0.3$ to 4 mm; (b) depicts the same data, zoomed in to emphasize sensitivities in the 0–50 mV (0– 10^{10} p/s) range.



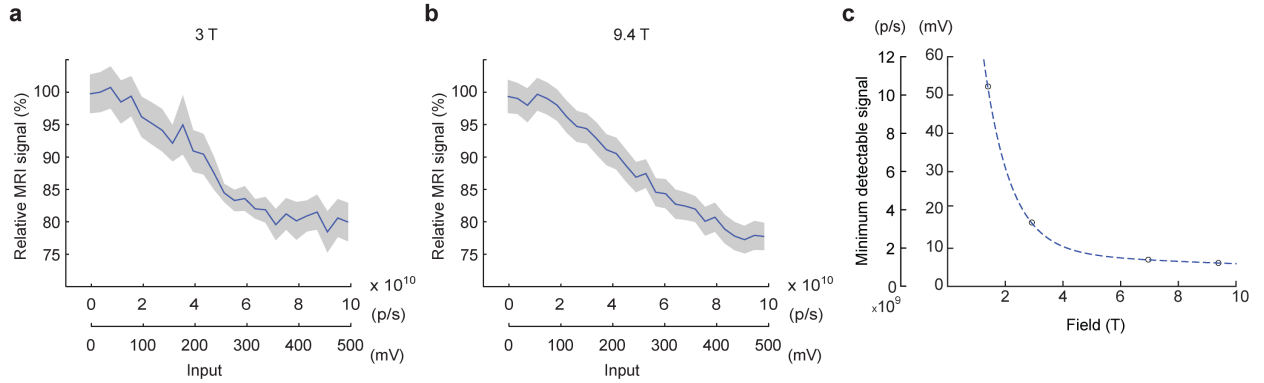
Supplementary Figure 4. Sensitivity of submillimeter multiturn ImpACT devices to voltaic and photonic inputs. Multiturn ImpACTs with diameters 1 mm, 500 μm , 250 μm , and 100 μm , can achieve 1% changes in B_{ImpACT}/B_I in response to inputs of -5.6 mV, -5.8 mV, -9.9 mV, and -33 mV, respectively.



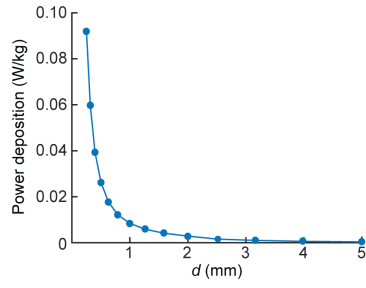
Supplementary Figure 5. Sensitivity of ImpACTs to biologically relevant fields. ImpACTs are initially tuned to resonance frequency of $\nu = 400$ MHz, in the absence of input at the FET closed state, and are detuned by input to gate electrode. **(a)** Application of voltage above V_{th} detunes the device and decreases Q (tuning curves at top), causing a reduction of MRI signal (images at bottom). ΔV_{GS} values shown for each condition, and 400 MHz frequency denoted vertical dotted lines with each tuning curve. **(b)** Photonic input from 0– 10^{13} p/s into a photoFET-based ImpACT device produces similar responses as the voltage input in panel (a).



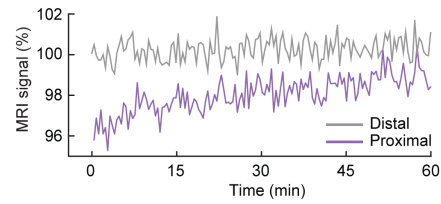
Supplementary Figure 6. ImpACT sensitivity to environmental changes. (a) Experimentally-determined dependence on ionic strength. A 3 mm ImpACT was initially tuned to resonance frequency $\nu = 400$ MHz and juxtaposed to saline solutions of 60-200 mM. Graph shows tuning depth (dBV) at the resonance frequency for different molarity values. (b) Temperature-dependence of ImpACT responses to stimulation. Tuning behavior against a 150 mM saline sample was measured across the entire dynamic range of inputs at room temperature (22 °C, red) or 37 °C (blue). (c) Simulated ImpACT response profiles predicted for operation at small frequency offsets from the main field resonance frequency (400 MHz). Curves determined over a range of offsets from 399 to 401 MHz are superimposable, showing negligible effect of realistic field distortions of up to 2,500 parts per million.



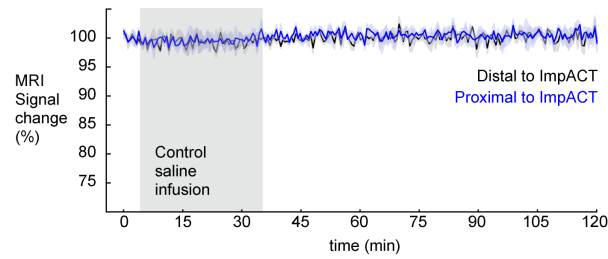
Supplementary Figure 7. ImpACT sensitivity at different MRI field strengths. (a) A 3 mm ImpACT tuned to $\nu = 123.2$ MHz was operated in a 3T clinical scanner over the full range of input amplitudes. **(b)** An ImpACT tuned to 400 MHz was similarly operated on a 9.4 T scanner. Shading denotes s.e.m. over 8 voxels in proximity to the ImpACT. **(c)** Simulated sensitivity of ImpACT devices, defined as the input amplitude predicted to produce a 1% change in B_{ImpACT}/B_1 , as a function of magnetic field strength.



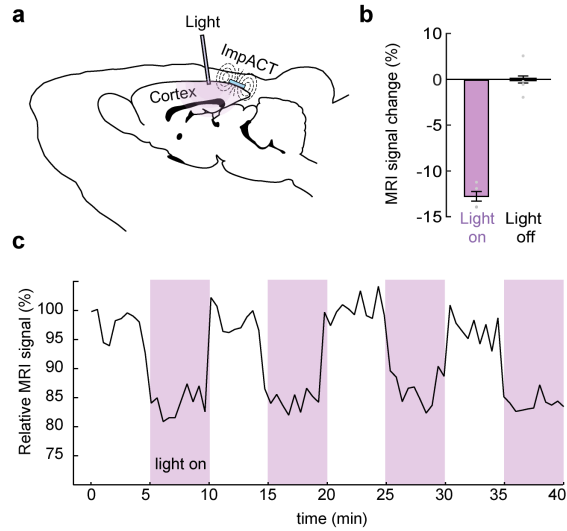
Supplementary Figure 8. Maximum local specific power dissipation by ImpACT devices. For ImpACT devices of different diameters (d), we calculated an upper bound on the local specific absorbance rate by computing the maximum specific power deposited in the ImpACT and then assuming that this power is transferred to a spherical volume of tissue of twice the diameter of the device (see Methods for details).



Supplementary Figure 9. Time course of relative MRI signal produced by NanoLuc-expressing cells. The graph shows time courses of NanoLuc-expressing HEK293 cells placed in close juxtaposition to an ImpACT device, following addition of 5 μ M furimazine. Signal close to the device (purple) shows relative suppression due to detuning of the device, compared with distal MRI signal (gray), which is not affected by the ImpACT or its tuning status.



Supplementary Figure 10. MRI monitoring of ImpACT response to sham injections of saline in live rat brains. Control experiments were performed as in Fig. 4g, but with injection of saline solution instead of furimazine. Engineered luciferase (NanoLuc)-expressing HEK-293 cells were grafted into the cerebral cortex and ImpACT device was implanted above the cells. An infusion cannula was inserted nearby for infusion of saline. Saline infusion ($t = 5-35$ mins) resulted in no significant signal enhancement in the center of the ImpACT device (paired t -test $p = 0.9309$) which remained tuned throughout the experiments. Mean time course depicts relative MRI signal proximal (blue) and distal (black) to the ImpACT (shaded margins denote s.e.m. over three animals). Saline infusion period indicated by gray box. Signal change axis spans 70-100 % as in Fig. 4g.



Supplementary Figure 11. Reversible detuning of an ImpACT device in live rat brain.

(a) A 3 mm photosensitive ImpACT device was implanted above the cortical surface of an anesthetized rat and an optical fiber was inserted 1 mm anterior to implantation site for light-dependent modulation. **(b)** Application of 5×10^{10} p/s generated MRI signal decrease of 12.7 ± 0.7 % in cortical region proximal to the device. Bars denote mean values, error bars denote s.e.m. ($n = 4$); individual data measurements indicated by gray dots. **(c)** Relative MRI signal proximal to ImpACT device in response to intermittent application of 5×10^{10} p/s through the optical fiber. Purple shaded areas denote 5 min epochs of light application.